Acta Materialia 159 (2018) 89–101

Contents lists available at ScienceDirect

Acta Materialia

journal homepage: www.elsevier.com/locate/actamat

Full length article

Crystallographic texture can be rapidly determined by electrochemical surface analytics

Alistair Speidel [a], Rong Su [b], Jonathon Mitchell-Smith [a], Paul Dryburgh [c], Ivan Bisterov [a], Don Pieris [c], Wenqi Li [c], Rikesh Patel [c], Matt Clark [c], Adam T. Clare [a, d, *]

[a] Advanced Component Engineering Laboratory (ACEL), Faculty of Engineering, University of Nottingham, NG8 1BB, United Kingdom
[b] Manufacturing Metrology Team, Faculty of Engineering, University of Nottingham, NG8 1BB, United Kingdom
[c] Optics and Photonics Group, Faculty of Engineering, University of Nottingham, NG8 1BB, United Kingdom
[d] Department of Mechanical, Materials and Manufacturing Engineering, Faculty of Science and Engineering, University of Nottingham China, 199 Taikang East Road, University Park, Ningbo 315100, China

ARTICLE INFO

Article history:
Received 10 April 2018
Received in revised form
24 July 2018
Accepted 24 July 2018
Available online 26 July 2018

Keywords:
Orientation mapping
Crystallographic characterisation
Electrochemical jet processing

ABSTRACT

Orientation affects application-defining properties of crystalline materials. Hence, information in this regard is highly-prized. We show that electrochemical jet processing (EJP), when coupled with accurate metrological appraisal, can characterise crystallographic texture. Implementation of this technique allows localised dissolution to be anisotropic and dependent on etch-rate selectivity, defined by the crystallography. EJP therefore, generates complex, but characteristic topographies. Through rapid surface processing and analysis, textural information can be elucidated. In this study, samples of polycrystalline Al and Ni have been subjected to EJP, and the resulting surfaces analysed to generate three-colour orientation contrast maps. Comparison of raw data acquired through our method with prior electron back-scatter diffraction data shows broad correlation and assignment (68% on a pixel-by-pixel basis), showcasing rapid large-area analysis at high efficiency.

1. Introduction

In polycrystalline materials, the distribution of grains and their absolute and relative crystallographic orientation has a profound impact on material performance, affecting factors such as fatigue [1], ultimate tensile strength [2] and creep [3]. Such information, regarding material texture and orientation is highly-prized as it serves to verify materials processing technologies. This understanding is especially important, particularly with the emergence of new manufacturing processes, seeking to further exploit orientation-specific material properties [4].

At present, the range of tools for determining the texture and orientation of material microstructure is limited. Orientation characterisation is commonly undertaken through diffraction-based techniques, such as electron back-scatter diffraction (EBSD) [5–7], transmission electron microscopy (TEM) techniques [8–10] and reflected electron techniques [11]. All of these rely upon electron diffraction and can characterise space group symmetries in an unambiguous manner, with lateral resolutions of <20 nm in some variants of EBSD [12], and smaller still with TEM techniques. However, their application is limited due the nature of analysis, and the use of electrons requiring high-vacuum equipment. In addition, sample preparation time and cost for EBSD and TEM specimens is often prohibitive and characterisation efficacy is dependent upon specimen quality. Large area analyses (mm scale) are impractical using TEM and encumbered by significant processing times in EBSD, despite increasing computational and processing efficiency [13]. Orientation characterisation of crystalline materials, under ambient conditions, is possible using X-rays to generate transmitted and back-reflected Laue patterns [14], although limited to single crystals. Novel methods for crystallographic characterisation, such as spatially resolved acoustic spectroscopy (SRAS), address these issues by eliminating vacuum equipment, reducing sample preparation time and are more suitable to large area appraisal than EBSD [15]. However, the resolution is presently limited by applied optical configurations and orientations for grains <50 μm have not been resolved, limiting the materials compatible with the technique.

* Corresponding author. Advanced Component Engineering Laboratory (ACEL), Faculty of Engineering, University of Nottingham, NG8 1BB, United Kingdom.
E-mail address: adam.clare@nottingham.ac.uk (A.T. Clare).

https://doi.org/10.1016/j.actamat.2018.07.059
1359-6454/

Materials characterisation techniques involving optical measurements are more amenable to rapid manufacturing strategies than electron measurements [16]. This has led to notable contributions considering the adaption of optical measurement techniques to acquire valuable microstructural information such as grain boundary character [17] and partial orientation information [18]. Such techniques exploit the differential reflected intensity of light, acquired under different lighting conditions, or using a goniometer setup. Rapid orientation measurement has also been achieved for silicon-based materials through alkaline etching and optical imaging [19], where simulations were fit against micrographs to elucidate crystallographic information considering the highly selective etching characteristics of silicon in hydroxide solutions.

This study reports on the creation of a novel tool for determining partial grain orientation, when calibrated against a conventional approach. This method is based on electrochemical jet processing (EJP) [20] for the selective anisotropic electrochemical etching of differently oriented grains. When coupled with appropriate metrology and processing, the technique holds several advantages over conventional methods and other reported optical methods, which make application of the process attractive from an industrial perspective. The analysed surface is rapidly generated in the dissolution process, eliminating specimen preparation time. Modern 3D optical profilers are capable of characterising topographies from above in a single measurement, reducing analysis time and cost. No significant sample preparation is required before analysis and the process can be executed on rough and undulating materials. In addition, discrete areas can be selectively appraised, compared with chemical bath etching, allowing the method to be used to verify materials processing techniques. From a practical perspective, it is shown that orientation-dependent topographies can be generated using solutions of cheap non-toxic salts, without corrosive chemicals. Furthermore, the presented technique is entirely scalable should the practitioner seek to characterise larger objects; there is no fundamental limit to the topography generation process.

This investigation shows the surface topography exposed by EJP to be consistent with long-range crystallographic order, under appropriate conditions. For anodic dissolution techniques, such as EJP, material is removed atomistically [21], where the remnant material crystallography is not altered, due to the athermal nature of the dissolution process, making EJP an ideal candidate for characteristic topography generation. This contrasts with other etching methods, such as thermal etching, which may alter the grain size and stress condition of the workpiece, depending on the material. Removal anisotropy is related to passivation characteristics of the different planar families [22]. Orientation-dependent featuring has been observed in pitting corrosion studies, for both Al [23] and Ni [24], where pit formation and propagation is dependent on localised chemistry within pits, the potential [25,26] and the resulting dissolution flow [27,28].

In crystallographic pitting, information regarding the underlying microstructure is contained within the surface topography [29]. While material degradation mechanisms have been explored, the utilisation of this information for microstructural characterisation is yet to be undertaken. Pitting phenomena are strongly affected by the incident electrolyte, which has also been widely studied. Passivating electrolytes, such as NO_3, most often used in EJP, are characterised by a tendency to generate oxide films during processing [30,31]. For micromachining, this allows enhanced dimensional accuracy [32], and brighter, pit-free surfaces [33], which is undesirable for the purpose of crystallography-driven topography generation. Conversely, aggressive electrolytes, such as Cl, lead to passivity breakdown, pitting, and reduced dimensional accuracy [34]. In this study, Cl-based electrolytes are shown in EJP to generate measurable orientation-specific topographies rapidly and across large areas in a controlled manner.

2. Materials and methods

2.1. Specimen preparation

Commercially pure Al 1050 (Smith's Metals UK), as well as Ni 201 and 6082 Al alloy (Unicorn Metals UK) were used in this study (all ≥98% purity). Sample pieces were subsequently annealed (Ni 1050 °C, Al 520 °C) for 3 h prior to grinding and polishing (1 μm diamond). For samples appraised by EBSD, further polishing was undertaken using colloidal silica (0.3 and 0.06 μm sequentially), before washing successively in ethyl lactate, acetone, methanol and isopropanol.

2.2. Surface generation

Equimolar solutions of NaCl and $NaNO_3$ (2.3 M) were prepared in deionised water from salts (Sigma Aldrich UK, and Fisher UK, respectively), and used as the electrolytes in this study. A bespoke CNC 3-axis EJP platform was used in this study, outlined in previous work [20]. Pits were drilled into materials across a range of current densities ($J_{noz} = 20–450$ A/cm^2), where the total charge passed was fixed (0.56 C per pit), through adapting machine time for a given current density. In all experiments, inter-electrode gap was kept constant (500 ± 1 μm). Large-area analysis was undertaken through a planar machining approach at constant translation speed (500 μm/s) and J_{noz} was maintained throughout machining (Al 6082, 50 A/cm^2; *cp* Ni 30 A/cm^2). Nozzle step-over was also maintained in each processing operation (Al 6082, 250 μm; *cp* Ni 500 μm). Samples were subsequently cleaned in deionised water in an ultrasonic bath, and characterised without further preparation.

2.3. Orientation mapping

A custom-built SRAS setup, was used to characterise the orientations of large areas of Al and Ni. In this case, a broadband Q-switched laser (1064 nm) and an optical mask, a grating pattern of known period, λ_g, were imaged onto each sample, matching the temporal frequency and spatial frequency of the laser and sample for narrow band excitation. The thermo-elastic effect caused by laser irradiance produces a packet of surface acoustic waves (SAWs) with a characteristic frequency, f_s. Thus, the velocity of the SAW, which is a function of the mechanical properties of the sample is found by $v_s = f_s\lambda_g$ [35]. The surface perturbation due to the SAW packet was detected by a knife-edge detector, using a second continuous wave laser (532 nm). All scans in this work were conducted at 24 μm wavelength, λ_g, giving a patch size of ≈200 μm and a nominal resolution of ≈100 μm. EBSD (Oxford Instruments HKL Advanced EBSD system, with NordlysMax3) was used to characterise orientations of a large-area of Ni prior to EJP (field of view, FOV: 4.85 × 3.63 mm, 4.5 μm/pixel).

2.4. Orientation-topographic analysis

Secondary electron and back-scatter electron microscopy (both Philips XL-30 SEM) were used to appraise surface textures after EJP. Focus-variation microscopy (Alicona G5 Infinitefocus, 50× and 100× objectives, FOV 324 × 324 μm and 160 × 160 μm, respectively) was used to qualitatively appraise topography including form and to evaluate root-mean-square (rms) surface roughness, *Sq*, per current density level. *Sq* was appraised after form removal (2nd order polynomial) and subjected to high-pass filter (at cut-off

spatial wavelength of 80 μm). A coherence scanning interferometry (CSI) instrument (Zygo NewView™ 8300, 50× objective, FOV 167 × 167 μm) was used to obtain accurate topographical information, from which surface gradient information was calculated. The characteristics of the processed surface determined by the orientations of crystalline grains were analysed based on the magnitude and direction of the gradient of surface height. The CSI system has been carefully calibrated, of which the surface topography repeatability is of the order of 0.1 nm and the step height accuracy is below 0.3% of the measured height [36–38]. Given accurately measured topography, the gradient vector of the surface can be easily obtained from the directional derivatives of the height map as

$$\mathrm{grad}(h) = \begin{bmatrix} g_x \\ g_y \end{bmatrix} = \begin{bmatrix} \partial h/\partial x \\ \partial h/\partial y \end{bmatrix},$$

where h is the height function of a surface, g_x and g_y are the partial derivatives of the height function in x and y directions, respectively. The direction of the gradient, at a given point on the surface, calculated as

$$\theta = \tan^{-1}\left(\frac{g_x}{g_y}\right),$$

is the orientation in which the gradient has the largest value (gradient magnitude) calculated as

$$|\mathrm{grad}(h)| = \sqrt{{g_x}^2 + {g_y}^2}.$$

In this work, the calculation of the gradient is done by numerically convolving the Sobel kernel with the height map of the surface [39]. The gradient direction, θ, ranges from −180° to 180° measured anticlockwise from the positive x-axis. Then the 2D map of the surface slope angle is calculated from the magnitude of the gradient as $\tan^{-1}(|\mathrm{grad}(h)|)$.

3. Results

3.1. EJP generates large-area orientation characteristic topographies

To characterise EJP-generated orientation-dependent surfaces, samples of polycrystalline Al and Ni were appraised using SRAS, to output crystallographic orientation maps [35], shown in Fig. 1b and c. From these datasets, discrete grains were identified, such that a pit was selectively machined into a grain vicinal to each of the three principal cubic orientations relative to the normal direction (ND) (Fig. 1a), using Cl electrolyte at a constant current density (20 A/cm^2). Location coordinates were imported into computer aided manufacturing software to generate a machine toolpath, with which the samples were subsequently processed. Secondary electron micrographs show textural variation associated with different orientations. Where grain orientation tends towards <001>, smooth surfaces are generated in Al in the central pit region (Fig. 1d) and a small number of cubic crystallographic pits are observed. Large gradients, approaching 90°, relative to the transverse direction (TD), (Fig. 1a), are seen in this orientation (Supplementary Fig. 1), resulting from retardation of dissolution in <001> directions, correlating with previous studies [40,41]. Here, resulting topography is defined by inhibited-etching directions. In Ni, surfaces are generated from repeating inverted square-pyramidal pits, when grains vicinal to [001] are machined (Fig. 1 e and f). The pyramidal walls generally feature gradients of between 30 and 40°, relative to the ND, indicating that for Ni, preferential removal is likely to be arrested by <111> directions (theoretically, $\tan^{-1}\frac{1}{\sqrt{2}}$, from ND, Supplementary Fig. 2).

For grains oriented towards <101> relative to the ND, repeating stepped features are generated in both Al and Ni (Fig. 1g and h), however the topographies are characteristic for each material. In Al, the inter-step angle is approximately 90° in this orientation, again indicating material removal retardation in the <001> directions. Conversely for Ni, grains tending towards [101] feature relatively large plateaus, which are indicative of a tendency towards an equilibrium removal condition. These areas are truncated by stepped features (Fig. 1h), the angle between the two surfaces being >90°, generally between 125 and 140° (Supplementary Fig. 3). Blunted diamond-like pits shown for Ni ≈[101] surfaces (Fig. 1i), previously reported in Ni [42], appearing to result from inhibited dissolution along <111> directions, theoretically $\tan^{-1}\frac{1}{\sqrt{0.5}}$, from ND (Supplementary Fig. 3). This indicates that dominant material removal follows <001>, and dissolution is inhibited along the <111>, and possibly <101> directions. Lower selectivity between <111> and <101> directions complicates surface topographies of Ni compared with Al, although the surfaces remain characteristic.

For grains tending towards <111> relative to the ND, repeating pyramidal-type textures are observed in Al (Fig. 1j), which is expected considering slowest etching directions aligning with <001>. For a periodic pyramidal surface, we expect three dominant slopes, with 120° inter-separation. For Ni, surfaces are composed of plateaued triangular features, where the angle of each triangular plate ≈60° (Supplementary Fig. 4). This corresponds to removal arrested by <111> faces, which are equilateral when sectioned through this orientation. Hexagonal pit morphologies, reflective of the packing of this orientation, are observed (Fig. 1k and l).

The surface textures generated in both materials here are intuitive, when considering their origins in the respective geometries of the principal orientations, and are therefore characteristic for a given parent-grain orientation. In Al, implicit in the exposure of cubic and pyramidal features is arrested material removal along <001> crystallographic directions [43]. For Ni, characteristic topographies can be explained considering removal arrested mainly by <111> directions. These relationships can be quantified in a repeatable manner and underlying orientation information can be output, relating the apparent topography to the principal cubic orientations.

3.2. Manipulating topography

Grain-dependent topography succinctly demonstrates anisotropic material removal and is dependent on the material, applied energy, and electrolyte used. For Al and Ni, it is shown that the result of using aggressive Cl electrolytes in EJP, is grain-dependent texturing at low applied current density (J_{noz} <100 A/cm^2), where J_{noz} is a tophat approximation of the current density distribution Fig. 2a). Grain-dependent texturing here results from crystallographic corrosion phenomena across the machined area. Textural relationship with J_{noz} is demonstrated by differential surface texturing (roughness, Sq, over multiple grains), which was measured for both materials in aggressive Cl and passivating NO_3 electrolytes (Fig. 2b and c). For Al and Ni processed with Cl, a power-type regression between surface amplitude and current density is followed, across J_{noz} = 20–450 A/cm^2. Amplitude depends on diffusion layer thickness in anodic dissolution, whereby electropolishing is achieved at high current densities, and asperities act as field-focussing elements, increasing localised current to enhance their dissolution rate [45,46]. At low current densities (<100 A/cm^2), where the surface resulting from EJP is dominated by microstructure effects, relatively large amplitudes are generated

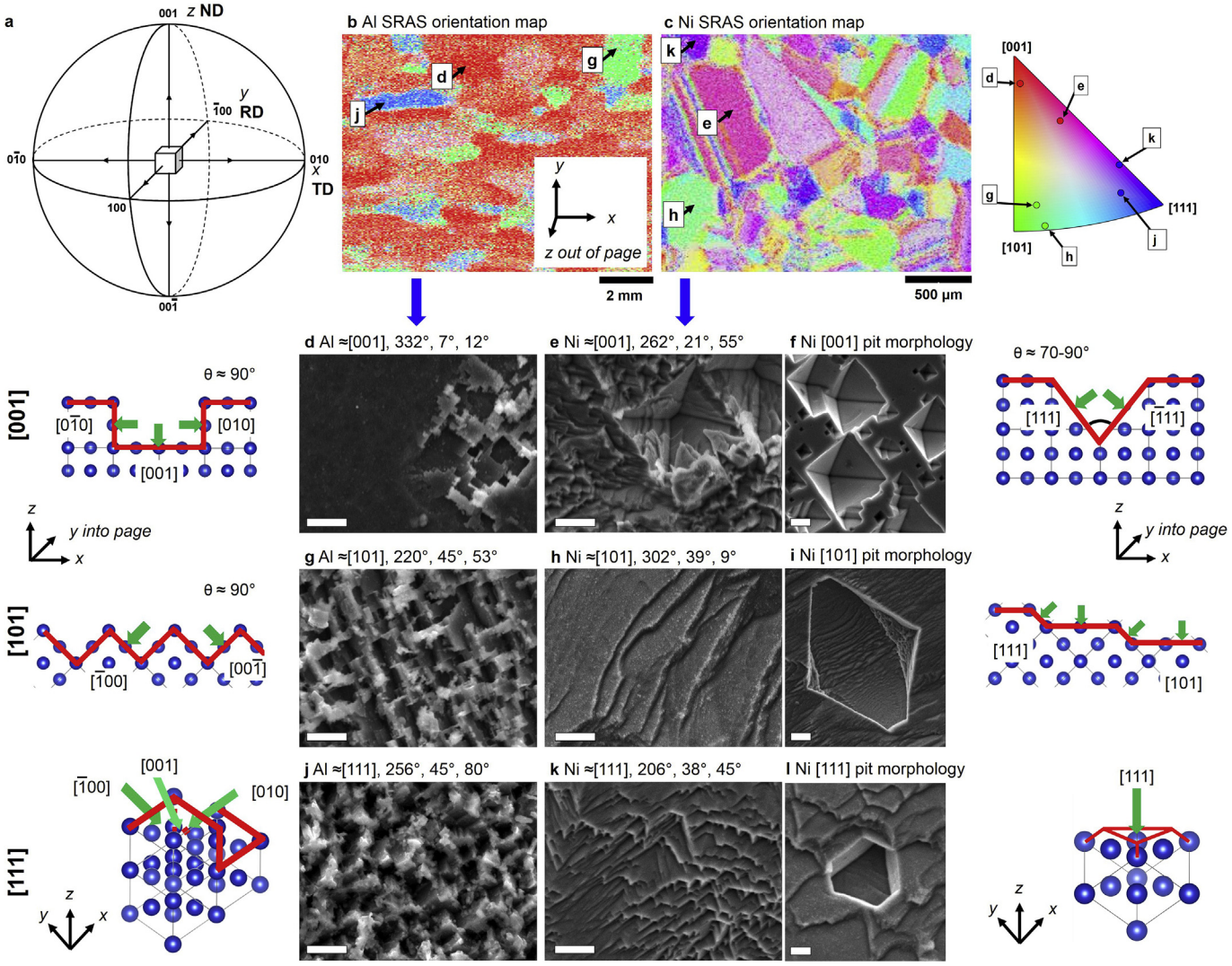

Fig. 1. Orientation defines microscale topography. For a cubic crystal system defined by Bunge notation [44] (**a**). From prior SRAS appraisal, orientation maps can be generated for both Al (50 × 100 µm/pixel) (**b**), and Ni (10 × 20 µm/pixel) (**c**). From these maps, grains were targeted, by inputting planar coordinates into computer aided manufacturing software, to observe topographic geometries resulting from the machining of grains of orientations relative ND, vicinal to the three principal cubic orientations ([001], [101], and [111]), at a current density of 20 A/cm^2). From the centres of the pits machined, differential textural geometries can be observed in the SE micrographs. For orientations vicinal to [001], in Al smooth surfaces, dispersed with cubic pits, are observed (**d**), in Ni, the surface is composed of coalesced inverted square-pyramidal pits (**e**), which are highly regular (**f**). For orientations vicinal to [101], stepped features are apparent in both Al (**g**) and Ni (**h**), although step angles tend towards 90° in Al, and 125° in Ni, implying that material removal could be bimodal in Ni at this current density and grain orientation. Pitting events are observed across single Ni [101] grains of Ni (blunt diamond morphology) (**i**). Where the grain orientation vicinal to [111], repeating pyramidal units can be observed in Al (**j**), and plateaued triangular features are seen in Ni (**k**). Hexagonal pitting events are detectable across the machined [111] oriented areas (**l**). These topographies are defined by the etch-inhibited directions (green arrows), for Al these are understood to be <001>, and for Ni the characteristic topographies can be generated by removal inhibition mainly of the <111> directions. All SEM scale bars are 5 µm. (For interpretation of the references to colour in this figure legend, the reader is referred to the Web version of this article.)

using Cl, indicative of the increasing scale of microstructure-defined topography. The scale of grain-dependent texturing is inversely proportional to the applied current density in EJP, between $J_{noz} = 20–200$ A/cm^2, beyond which the amplitude does not decrease significantly. For Al and Ni, we can enhance lattice-defined texturing at current densities <100 A/cm^2, hence operation within this domain is preferred. We did not observe equivalent amplitude relationships for these materials processed with NO_3, indicative of reduced dependence on the specimen microstructure. Topographic reconstructions, acquired after we machined across current densities: $J_{noz} = 20$, 50, 100, 300 A/cm^2, using Cl (Fig. 2d–r) correlate with the amplitude analysis, resulting in a gradual transition from microstructure-defined removal to electropolishing. Using NO_3 electrolyte under equivalent processing, we observed no lattice-defined topography in Al, and a limited extent in Ni, although less than with Cl (Supplementary Fig. 5), likely to be a result of the more positive oxidation potential: Ni < Al (*vs.* standard hydrogen electrode) [47]. In Al, anodic oxide-generating NO_3 delocalises material removal from the microstructure, hence etching is isotropic. Thus aggressive electrolytes, stimulating anisotropic removal in EJP, are preferable when characterising these materials.

The SEM micrographs (Fig. 2e–s) acquired at identical current densities (20, 50, 100, 300 A/cm^2), show single grain topographies. In this study, lattice-defined removal is demonstrated, resulting in cubic geometric structuring at current densities <100 A/cm^2 (J_{noz}), for both materials, the scale of which decreases as J is increased. For both materials studied here, processing at high current density (J_{noz} ≥300 A/cm^2) results in negligible periodic topography at this

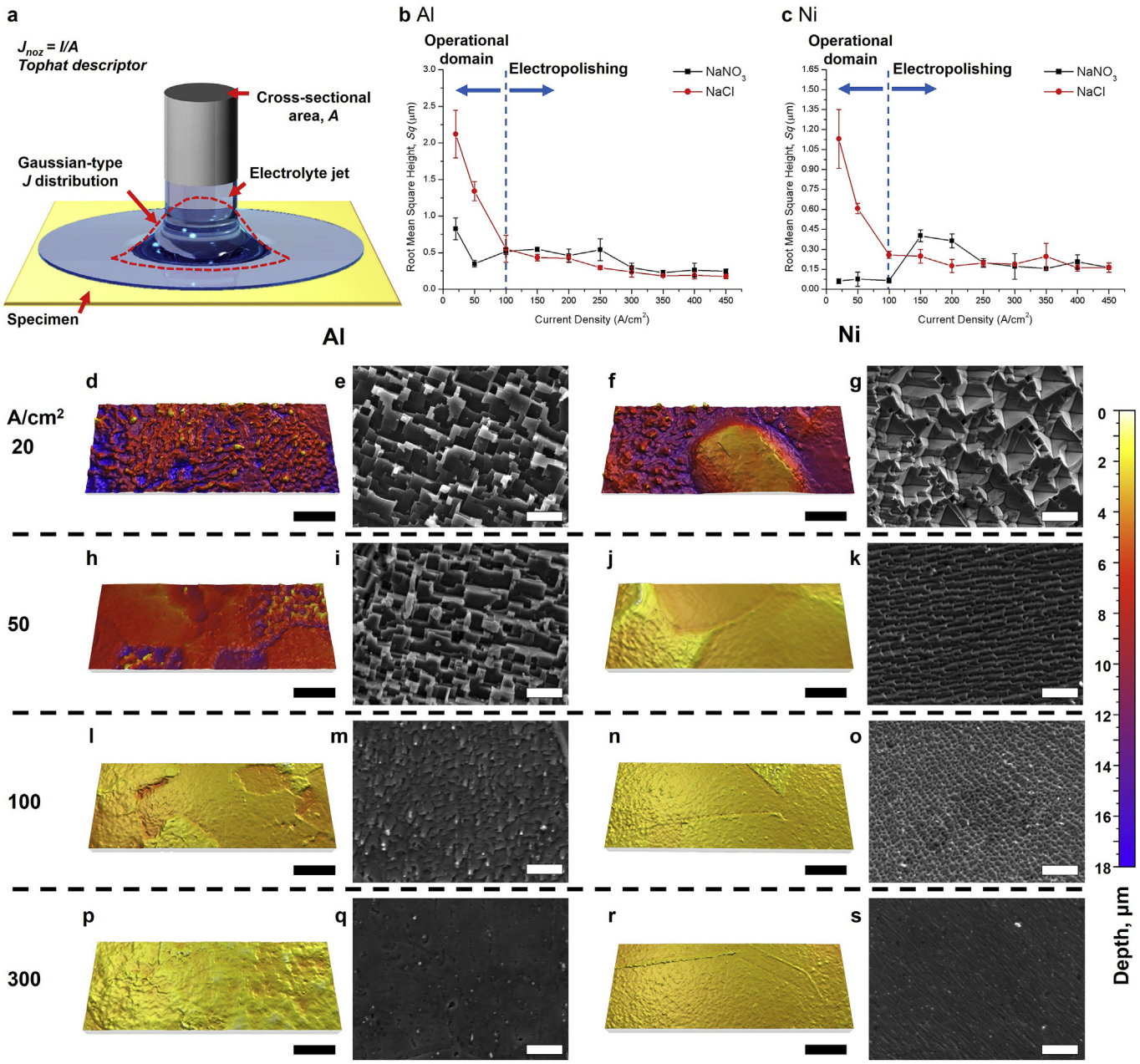

Fig. 2. The operational domain is defined by current density. Current density, J, exhibits a Gaussian-type distribution, where J_{noz} is a tophat approximation considering current, I, and nozzle area, A (**a**). RMS roughness, Sq, shown as approximate power regression with J_{noz}, for Al machined with Cl, but not upon machining with NO_3 (**b**), also observed for Ni (**c**). Reconstructions of EJP processed areas acquired using focus-variation (FV) microscope (50× objective), and subjected to 2nd order polynomial form filter [50]. SE micrographs of single-grain areas of the surface, machined with Cl. At low current density ($J_{noz} = 20$ A/cm^2), grain-dependent topography is generated in Al (**d**), and repeating microscale structuring is observed (**e**). For Ni, the same effect is shown (**f**), and repeating topographies are evident (**g**). Upon increasing current density ($J_{noz} = 50$ A/cm^2), grain-dependent topographic contrast is still evident in Al, although finer in scale (**h**), with ordered surface structuring (**i**). The same effect is observed for Ni (**j**), although the scale of the periodic structuring is reduced (**k**). At higher current density ($J_{noz} = 100$ A/cm^2) topography amplitude is reduced, but still apparent in both materials, such as for Al (**l**), and finer-scale repeatable surfaces are shown in SEM, although appearing to delocalise from high-level ordering associated with lower current densities (**m**), this effect is observed in Ni (**n**), and (**o**). At higher current densities (300 A/cm^2), no grain-dependent topography is observed in Al (**p**), and smooth surface textures are observed (**q**), the same is shown for Ni, although intergranular attack is evident (**r**), and some ordering is apparent (**s**). Electropolishing mechanisms dominate ≥100 A/cm^2. Error bars are the standard deviation of surfaces appraised, from three discrete pits for each data point. Black scale bars are 50 µm, white scale bars are 10 µm.

length scale. Transpassive dissolution of materials has previously been shown to have limited dependence on microstructural factors, such as orientation [48]. It is assistive to the technique that lattice-defined topography is largely insensitive to applied current density over a broad range (20–100 A/cm^2), even where transpassive dissolution modes are predicted, (Ni, $J \leq 20$ A/cm^2) [49].

When machining, the dissolution profile is dictated by the current density distribution. Classically, this appears Gaussian for a cylindrical nozzle, (Fig. 2a). Localised variation in microscale topography is observed as a result of the feature form, such as for Al vicinal to [001], where inhibited-etching directions, defined by the material-process response, follow <001>. A pit section is shown in Fig. 3a, where the central region appears reflective, indicative of lower surface amplitude, compared with the walls (Fig. 3b). At low

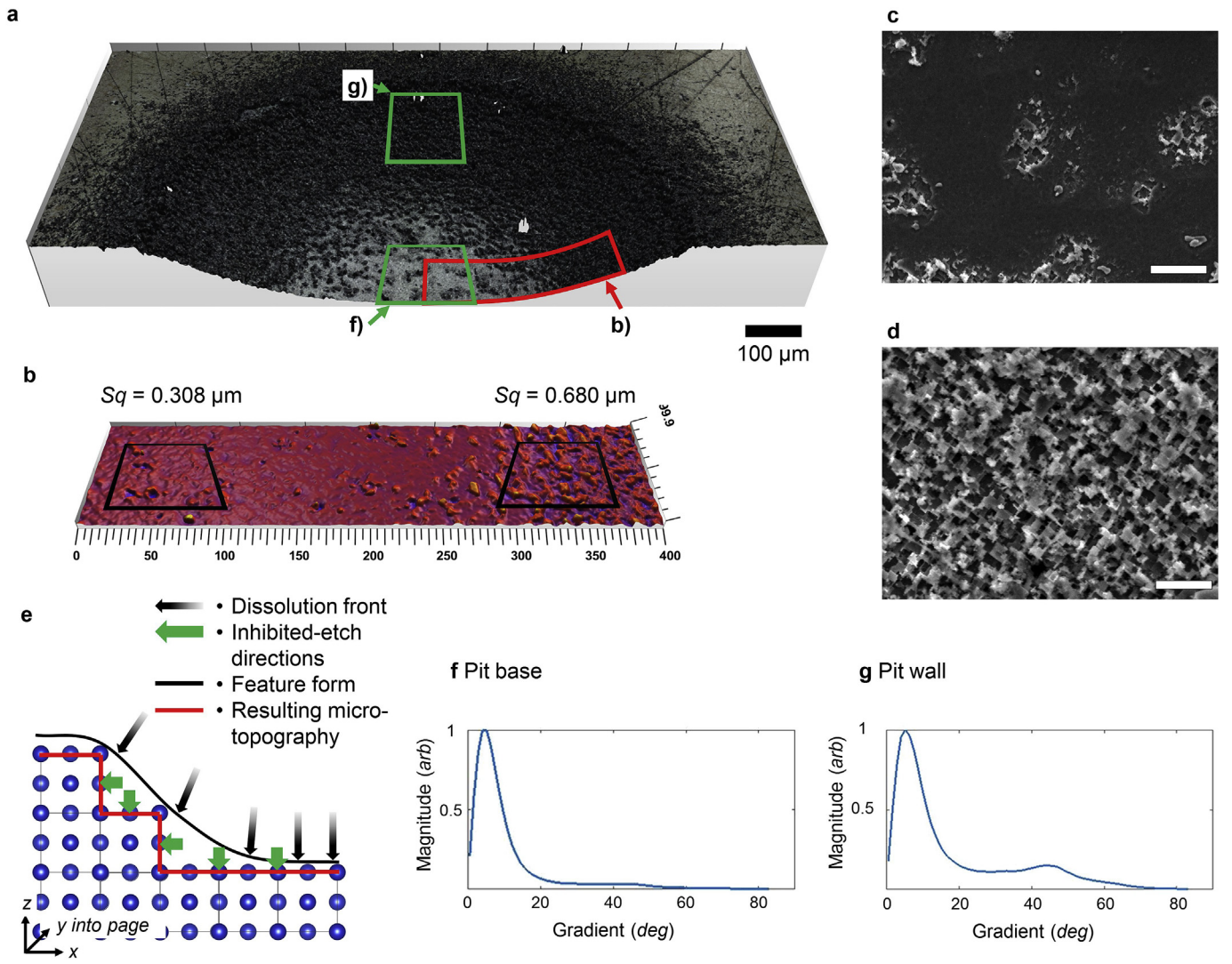

Fig. 3. Characteristic topography generation is independent of dissolution front. Reconstructed pit section, with optical micrograph (FV microscope, 50× objective) drilled at low current density (20 A/cm^2, 14 s dwell) into a single-grain area of Al (Cl electrolyte), orientation ≈[001], showing greater reflectivity at the centre, (extracted surface shown red) (**a**). From extracted surface (after form removal, 2nd order polynomial) the reconstruction shows differing RMS roughness, *Sq*, where the central region has a lower amplitude, and greater smoothness (**b**). Complementary secondary electron micrographs, showing differential texturing observed at the pit base (**c**) and side (**d**), where equivalent cubic recesses are observed, albeit at a finer surface dispersion in the pit base. This can be correlated with the relationship between the dissolution front and the etch-inhibited directions (**e**). Gradient magnitude plots for the pit base (**f**) and side (**g**), showing a similar low angle peak regardless of pit form. SEM scale bars 10 μm. (For interpretation of the references to colour in this figure legend, the reader is referred to the Web version of this article.)

J, smooth surfaces are not generally expected in EJP [46]. Despite differential amplitudes, similarities in the textural morphologies at the pit base and the side wall are observed Fig. 3b c and d).

An interpretation of the surface-generation mechanism for Al is shown in the idealised schematic in Fig. 3e. As dissolution achieves steady-state and a side wall of the pit becomes exposed, additional <001> inhibited-etch directions are exposed. Therefore, the topography generated is inconsistent with that subject to attack from the normal direction. While the topography created throughout the pit is not uniform, this does not present significant challenge to the succeeding analysis method, which accommodates this variation. This is evidenced by the complementary gradient magnitude plots in Fig. 3f and g, wherein a large low-angle peak <10° is observed regardless of the feature form, correlating with the flat exposed <001> facets. Dominant slope angles are similar at the pit base and the side walls, as these are defined by equivalent inhibited-etch directions, however surface dispersion of cubic pits is lower at the base. Material removal not occurring in the normal direction in this case, leads to periodic surface stepping, scattering more light, therefore appearing dull to the observer. Since characteristic slope angles are the same at the base and side of the pit, they remain representative of the underlying grain orientation. The dependency of the micro-topography on the feature form is therefore reduced, under anisotropic etching conditions.

When creating striations through jet translation, the same effect is observed, shown for Ni, where the orientation was evaluated by SRAS prior to EJP (*see* Fig. 4a). Translation EJP reveals grain-dependent topography, shown in the optical micrograph in Fig. 4b, where surfaces of grains vicinal to [001] appear dull to the observer, due to the theoretical inverted pyramidal microscale topography (*see* Fig. 1e), and surfaces of grains vicinal to [111] appear bright, due to the expected plateaued areas. Periodic form over the surface correlates with nozzle diameter and is controlled by the Gaussian energy distribution (*see* Fig. 4c). Topographies from a single-grain area, corresponding to an

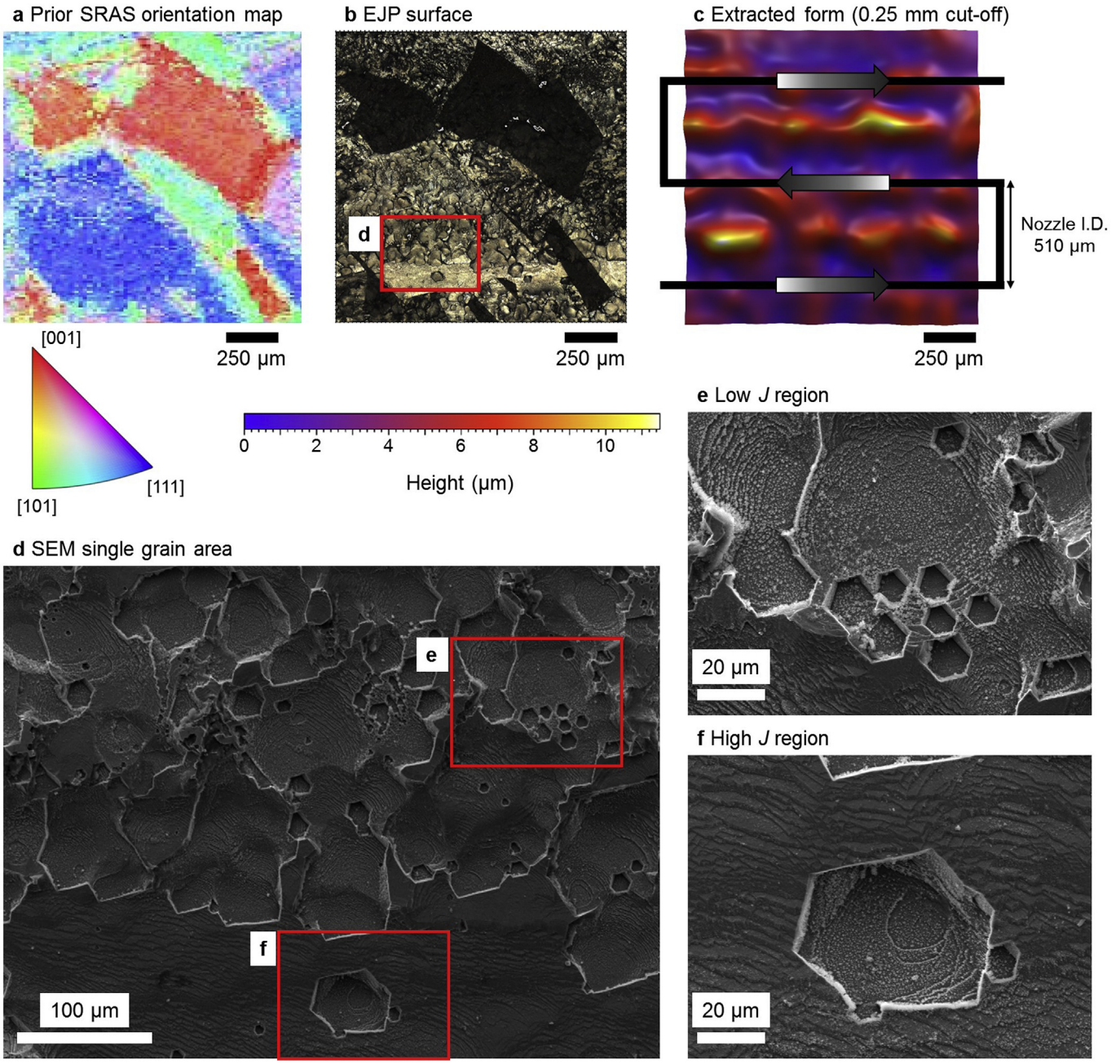

Fig. 4. Large areas can be processed using a planar scan strategy. From prior SRAS orientation data (18 directions, 20 × 10 µm/pixel), the large grain vicinal to [111] (blue) was considered (**a**). The surface was etched with EJP (30 A/cm^2, $v_h = 0.5$ mm/s), to reveal grain-dependent texturing, where the visible optical contrast can be correlated with grain orientation (**b**). The topographic form was extracted (0.25 mm cut-off), whereby the periodicity is directly related to the nozzle diameter (**c**). SE micrographs (**d-f**), showing similar microscale texturing in the low and high *J* regions of the translating jet, although pit frequency is greater in the low *J* region. (For interpretation of the references to colour in this figure legend, the reader is referred to the Web version of this article.)

orientation vicinal to [111] as indicated in the SRAS orientation map, show equivalent characteristic microscale texturing at central and edge regions of the resulting EJP slot. This is evidenced in the SE micrographs (*see* Fig. 4d–f). Pitting frequency is inversely related to the applied current density, however it should be noted that the succeeding analysis routine does not consider discrete pits, rather the larger area microscale surface structuring. Similar topographies are observed despite the total surface amplitude being greater in the low *J* region. Consistency of micro-topography generated, largely independent of form, allows significant areas to be rapidly processed and characterised (with no fundamental limit).

3.3. Surface analytics

The topography of jet processed surfaces varies within single-grains, due to the lattice orientation relative to the dissolution front. However, surface characteristics unique to given orientations in both Al and Ni, are revealed by the gradients of the resulting topography. Using CSI, the gradient vector of the surface can be obtained from the directional derivatives of the topographic data-set (*see* methodology), showing a statistical distribution of the characteristic slopes for a given surface. Subsequently, the two-dimensional map of the slope angle is calculated from the magnitude of the resulting gradient vector, and the gradient direction at

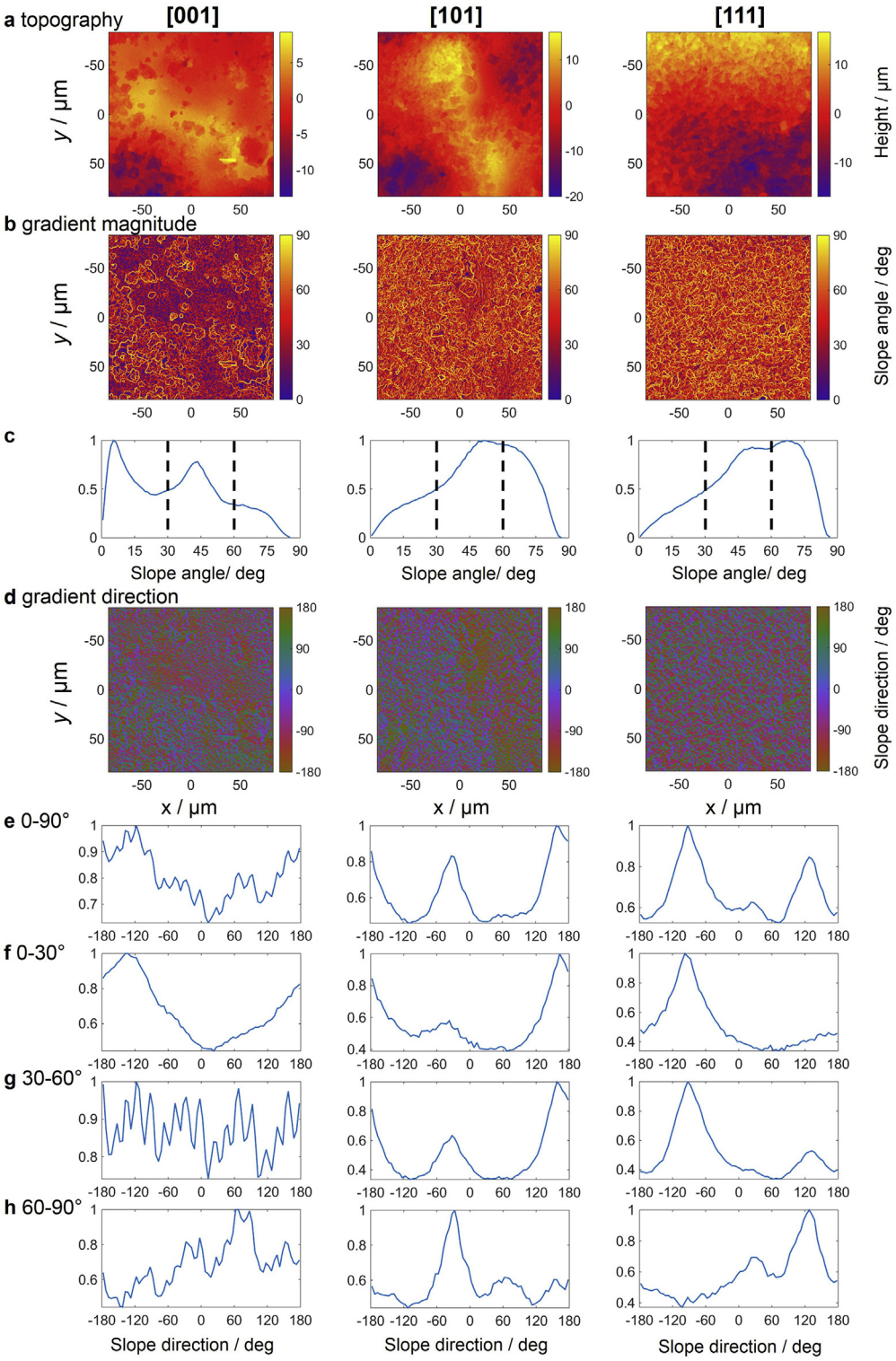

Fig. 5. Surface analytical correlation in Al. For Al grains oriented vicinal to the three principal cubic orientations. Datasets showing raw CSI topography (50× objective), shown for ≈[001], ≈[101] and ≈[111] (**a**). From these datasets, slope magnitude can be appraised, revealing the gradient maps for the prior topographies vicinal to: [001], [101] and [111] (**b**). Corresponding statistical analysis shows a low angle peak for grains oriented ≈[001] (significant flat surface), and similar dominant slope angles >45° for orientations vicinal to [101] and [111] (**c**). These textures are separable through analysis of the slope direction, which reveals two-dimensional gradient direction maps for vicinal [001], [101] and [111] respectively (**d**). Statistical analysis of this data shows that for ≈[001] oriented grains, the distribution is unstable (due to the plateaued topography of the surface), for grains ≈[101], where stepped surfaces are generated, two dominant peaks are observed, the difference between the directions is 180°, and for grains vicinal to [111], three dominant peaks are observed, the direction separated by 120° (**e**). Windowing of the gradient distribution can reveal more topographic information, for low angles (0–30°): ≈[001] shows one dominant direction, while ≈[101] and ≈[111] show two dominant directions (**f**). For higher angle gradients (30–60°), periodicity, defined by the cubic geometry of the surface is observed for ≈[001], although no significant difference in the dominant peaks is shown for ≈[101], or ≈[111] (**g**). Windowing high-angle gradients (60–90°), periodicity is still apparent for ≈[001] grains, two additional peaks are apparent for ≈[101] grains, separated by 90° (Supplementary Fig. 1b) and for ≈[111] oriented grains, the second and third peaks are clearly observed, still separated by 120° (**h**).

each point on the surface that is pointing in the direction of the steepest slope at that point. Here, the Sobel kernel [39] is used to conduct the numerical calculation, and the gradient direction ranges from −180° to 180°, where the angle measured anticlockwise from the positive *x*-axis (defined as 0°) is positive and the angle measured clockwise is negative.

From this distribution, the gradient directions can be quantified, yielding a distribution of peaks unique for an orientation in a given material. For Al grains oriented vicinal [001], micro-topographies comprised of cubic recesses are generated under anisotropic electrochemical etching conditions, (repeating flat areas). This means small slope angles (<10°) are prominent (Fig. 5c). In this case, the gradient direction varies and trend observation is difficult. For orientations vicinal to [101] and [111], further analysis is necessary for differentiation, through analysis of slope direction, as the histograms for both of these surfaces show similar prominent slope angles which are >45°. For a stepped topography representative of that observed for etched grains orientated vicinal [101], the theoretical difference of peaks is 180° (Fig. 5e). When grains vicinal [111] are subjected to EJP, periodic pyramidal topographies are observed. The theoretical angle in this case will be 120° (Fig. 1j). Where the peak separation is >160° - <190°, the sample surface assigned to [101], and where the peak separation is >100° - <130°, the sample surface is assigned to [111]. For surfaces where neither of these criteria are satisfied, such as a strongly hybridised texture, or an area of unprocessed surface, the sampling area is set as a non-measured point (see Fig. 6).

For Ni, EJP-generated surfaces are more complex, resulting from lower anisotropic etching, hence contrasting is more challenging. The inverted square-pyramidal pitting seen resulting from EJP of orientations vicinal [001], means that the dominant slope angle will be ≤45°. In addition, the slope directions of the pyramidal features are separated by 90°. For grains oriented vicinal to [101], the histogram shows a dominant peak between 10 and 20°, along with a smaller peak between 30 and 40°. In addition, the separation of the slope directions is >120°. For grains oriented vicinal to the [111], the histogram shows a dominant slope angle <10°, corresponding to plateaued areas. Characterisation of the slope directions in this case shows three directions with a separation of 120°. Both [101] and [111] surfaces show six major slope directions for high-slope surfaces (60–90°).

Through applying this method, a grain of Al or Ni can be readily assigned to the closest principal orientation. Automating data acquisition and analysing topographical information allows planar response profiles to be plotted to generate three-colour orientation texture maps. Equivalent orientations generate identical characteristic slopes from identical EJP treatment and the aforementioned topographical analysis. However, since this characterisation intervention is far less than conventional methods, the technique is deployable upon high-value assets beyond the laboratory. Nonetheless, it is intuitive that reciprocal orientations lead to machined surfaces with characteristic alignment relative to the normal and transverse directions. Analysis of absolute gradient directions may be applied to increase the measurement fidelity.

3.4. Crystallographic texture mapping, validation and error

Grain orientation texture maps were generated for Al and Ni specimens and are shown in Fig. 7. Comparing with prior SRAS orientation data (Supplementary Fig. 6a) in Al, surface processing reveals grain-dependent topography evidenced by the optical micrograph in Fig. 7a. This surface was measured using CSI (<20 s per 167 × 167 μm acquisition) and the aforementioned characterisation routine, to output an orientation contrast map (Fig. 7b). To generate this map, each acquisition area was split into 16 discrete analysis regions, corresponding to a pixel size of 42 μm. SEM analysis of grain topographies show textures expected from the respective assignments in Al (Fig. 7c–f), demonstrating large-area method repeatability. In addition, clear boundaries are observed, where intergranular corrosion, where topography is not representative of the underlying orientation, is <2 μm wide (Fig. 7g and h), less than the sampling distance of this technique. For Ni, prior EBSD data (Fig. 7i), was down sampled to three-colours (Euler angles for each interrogated grain are shown in Supplementary Table 1), against which to benchmark the novel approach (Fig. 7j). The resulting output orientation map using this method is shown in Fig. 7k (42 μm per pixel). Validation was undertaken by down sampling EBSD data to the same pixel size as the output map. The two datasets were subsequently overlaid in Matlab, wherein they were subtracted; any value that did not correspond to zero was allocated mis-assigned. Conversely, zero values relate to direct correlation. The map is in broad agreement with prior EBSD data on a pixel-by-pixel basis (68% pixels correlate to EBSD) (Supplementary Fig. 7c) and crystallographic contrast is observed in the output map. Correlated pixel assignment was greatest for [001] textured grains (75%), followed by [101] (65%) and [111] (62%).

In order to realise the origins of uncorrelated pixels in the validation study, the Ni surface was inspected with SE microscopy (*see* Fig. 7l–o). Different causes have been identified leading to correlation discrepancy: 1) Material removal, where the revealed microstructure is not representative of the near-surface microstructure, measured by EBSD (≤50 μm of Ni was removed, Supplementary Fig. 8b), leading to shifting boundaries during etching, also the complete corrosion of grains. 2) Hybrid topographies of unpolarised grains not vicinal to any principal orientation. Bisecting grains are assigned as non-measured points in the output maps, although in some instances surfaces appear representative of the more dominant removal directions (such as Ni <001>). This could explain the bias of mis-assigned pixels from [101] grains to [001], ahead of slow-dissolving [111] (Supplementary Fig. 7d). 3) Grain-boundary effects, such as where stepped edges are generated, exhibiting [101]-characteristic topographies.

The difficulty in validating the novel method with conventional materials characterisation techniques such as EBSD is further evidenced in Fig. 8 (≈10.5 μm/pixel). The prior EBSD data was down sampled to the same pixel size accordingly (see Fig. 8a). Upon EJP, the shifting of the grain boundary zone and the removal of a grain is clearly shown in the subtracted overlay (*see* Fig. 8c). This contributes to the uncertainty, in correlation with prior EBSD data. In addition, it should be noted that a small proportion of the subtractive mis-assignment arises from non-measured points in the prior EBSD data (in the sample area, approximately 10% of the pixels in the prior EBSD data have returned as non-measured).

4. Conclusions

In this study, a scalable procedure has been defined allowing rapid assignment of crystalline texture under ambient conditions with minimal intervention, making the technique particularly amenable to large-area industrial application. Automation of data acquisition has been demonstrated, resulting in the ability to differentiate grains according to the three cubic principle crystallographic directions.

In addition, a route through which orientation-dependent topographies can be rapidly and selectively generated using non-toxic solutions is presented, without altering the crystallography of the material. In this regard, it is suggested that the EJP surface preparation technique could be assistive to other developing optical characterisation methods such as directional reflectance

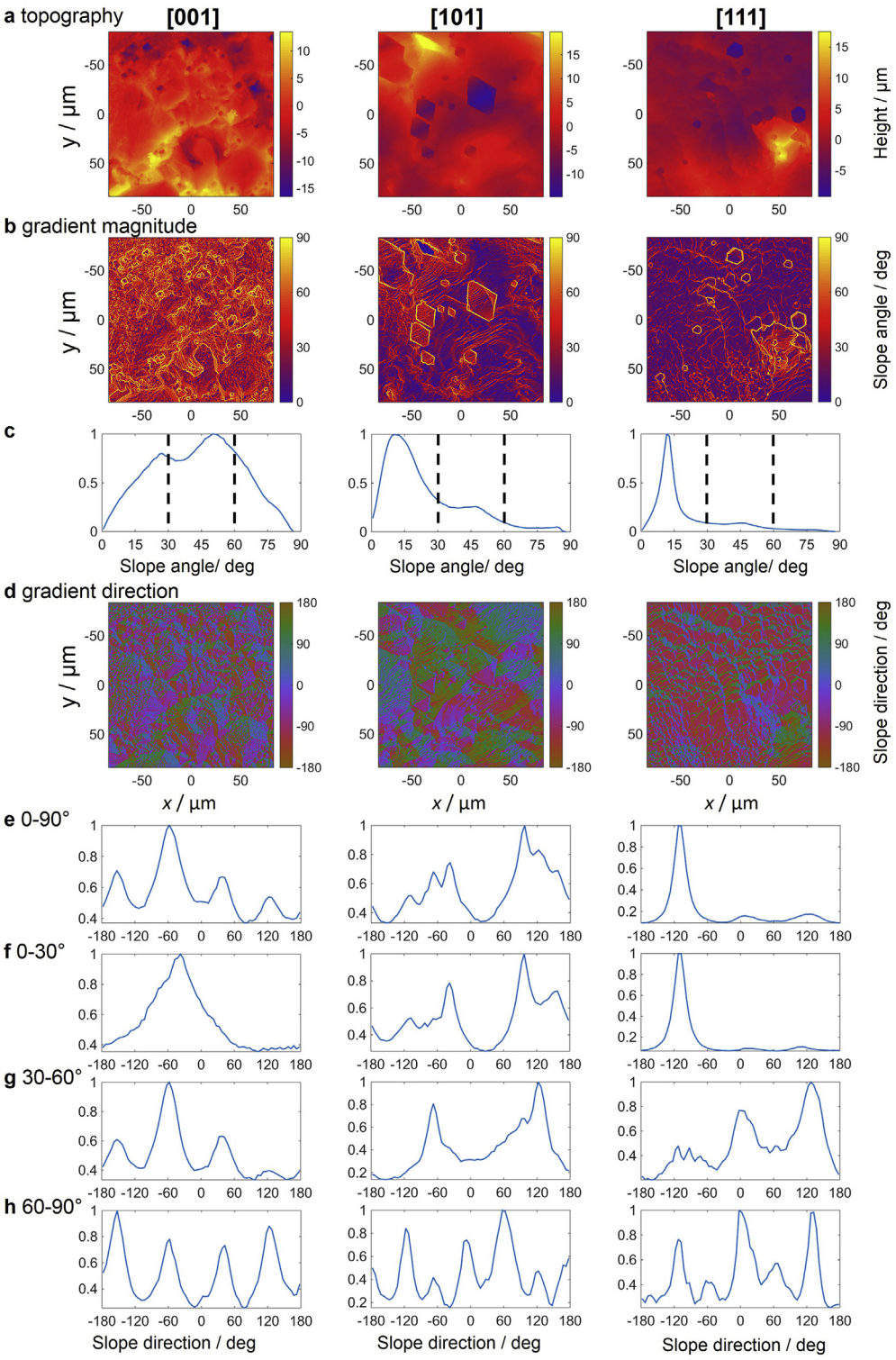

Fig. 6. Surface analytical correlation in Ni. For Ni, grains oriented vicinal to the three principal cubic orientations. Datasets of raw CSI topography (50× objective), shown for ≈[001], ≈[101] and ≈[111] oriented grains (**a**). Slope magnitude can be appraised reveal gradient maps for orientations vicinal to [001], [101] and [111] (**b**). Corresponding statistical analysis shows two broad gradients with angles of ≈30° and ≈50° for grains oriented ≈[001] (pyramidal topography). Orientations vicinal to [101] show a broad low-angle slope and a small peak ≈30–40° (correlating with periodic stepping). A similar distribution is shown for [111], although the low-angle slope is significantly narrower corresponding to large plateaus (**c**). Analysis of the slope direction, generates maps for [001], [101] and [111] (**d**). Statistical analysis shows for ≈[001] oriented grains, pyramidal slopes are separated by 90°, for grains ≈[101], where stepped surfaces with are generated, two dominant peaks are observed, the difference between the directions is >120°, and for grains vicinal to [111], three dominant peaks are observed, the direction separated by ≈120° (**e**). Windowing of the gradient distribution, for low angles (0–30°): ≈[001] shows one broad direction, while ≈[101] and ≈[111] surfaces show dominant directions statistically representative of the non-segmented direction distribution, as these cases, the majority of the slopes are low-angle (**f**). For higher angle gradients (30–60°), periodicity, defined by the pyramidal geometry of the surface is observed for ≈[001], for ≈[101] surfaces, ≈180° peak separation is apparent, and for ≈[111], the ≈120° peak separation is shown (**g**). Windowing high-angle gradients (60–90°), strong periodicity for ≈[001] grains is shown (reflective of the four-fold rotational symmetry of pyramidal features, six periodic peaks are apparent for ≈[101], and for ≈[111], reflective of the hexagonal packing of the inhibited-etch directions <111>, leading to the six-walled [101] (blunt diamond) and [111] (hexagonal) pits (**h**).

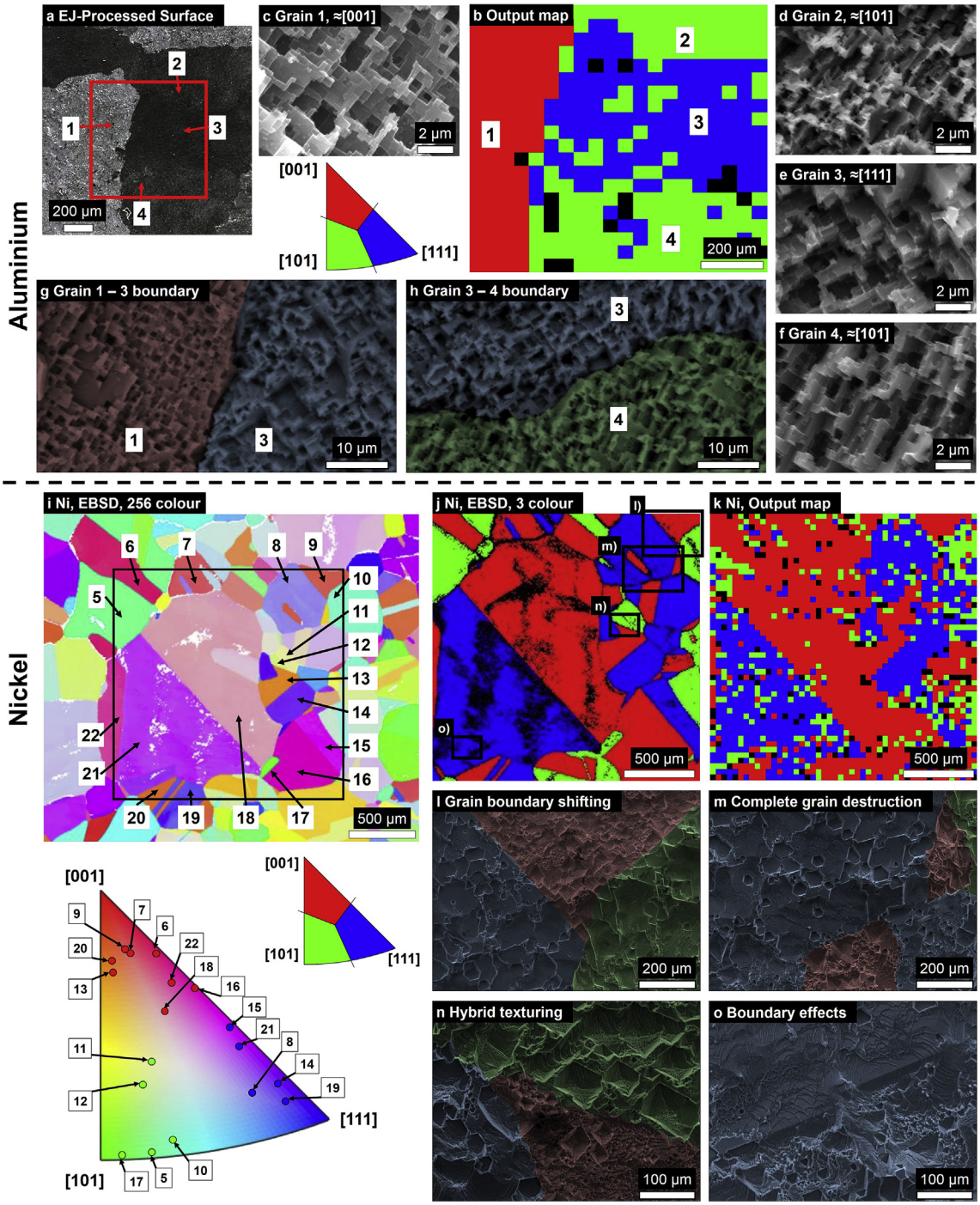

Fig. 7. Microstructural texture can be rapidly mapped using EJP over mm scale areas. For Al, optical micrograph of large-area EJP surface (inset red, CSI acquisition area 50× objective) (**a**). Topography orientation output map (42 µm/pixel) (red [001], green [101], blue [111], black – non-measured), where pixels are assigned to closest principal orientations (**b**). SE micrographs showing grain 1 topography, assigned [001] (**c**), 2, assigned [101] (**d**), 3, assigned [111] (**e**), 4, assigned [101] (**f**). Tinted micrographs showing boundary zones between grain 1 and 3 (**g**), and grain 3 and 4 (**h**), in both cases, the intergranular crevice is <2 µm wide. For Ni, appraised by prior EBSD orientation measurement (RGB dataset), CSI acquisition area black inset (50x objective), with labelled grains (**i**). EBSD data downsampled to three-colours, through bin assignment to the closest principal orientation for comparison, grains labelled as per inverse pole figure (**j**). Output planar texture map (42 µm/pixel, colour convention as Al), showing orientation contrast and correlation (68%) with prior EBSD data on a pixel-by-pixel basis (**k**). Three causes of non-correlated pixels are identified here: surface destruction, resulting in apparent grain boundary shifting (**l**) and complete corrosion of prior measured grains – the annealing twin within grain 8 is removed, and not assigned in output map (**m**); bisection of parent-grain orientation - texture shown likely to be grain 11 (after complete corrosion of grain 12), which has an orientation bisecting [001] and [101]. The method has assigned to [001], largely as a consequence of the inverted pyramidal topography (**n**). Mis-assignment caused by boundary effects: similar ≈[111] grain boundaries mis-assigned to [101]-type texturing, due to the large intergranular step (**o**). (For interpretation of the references to colour in this figure legend, the reader is referred to the Web version of this article.)

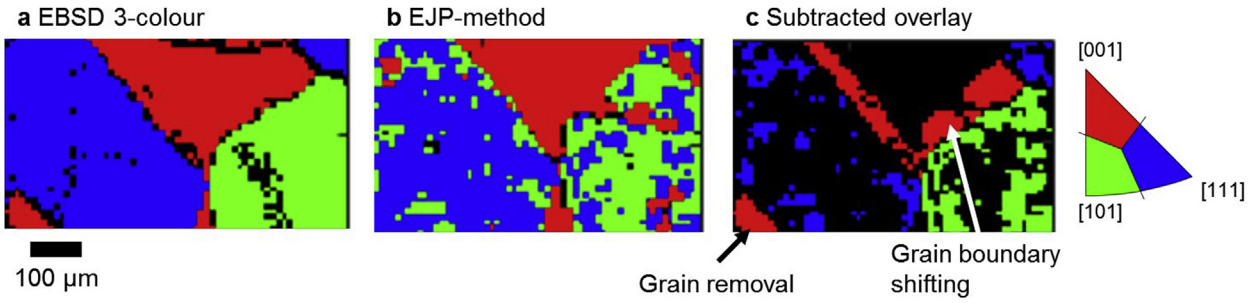

Fig. 8. One representation of validation difficulty. Comparing prior EBSD data (3-colour, 10.5 µm/pixel) (**a**) with the novel approach (**b**), the subtractive overlay shows the shifting of grain boundaries and grain removal as the exposed surface crystallography is discrete from the prior surface, measured by EBSD (**c**). Non-measured EBSD pixels are also shown to contribute to the mis-assigned pixels. (For interpretation of the references to colour in this figure legend, the reader is referred to the Web version of this article.)

microscopy [18]. Although a large degree of uncertainty is acknowledged and remains the subject of ongoing research within the group, it is hoped that the materials community will assist with the development of this technique into a more comprehensive method.

Enhancements in output data quality and correlation with EBSD can be achieved using simple filtering operations, although care was taken to present only raw datasets in this study. Further enhancement of the polar resolution and crystal class identification is possible by considering absolute gradient directions, as well as hybridisation characteristics of unpolarised (to the principal cubic directions) grain topographies.

Acknowledgements

This work was supported by the Engineering and Physical Sciences Research Council [grant numbers EP/R511730/1, EP/L016206/1] through the "Impact Accelerator Account – University of Nottingham (2017)", and the EPSRC Centre for Doctoral Training in Innovative Metal Processing, and by the European Metrology Programme for Innovation and Research (EMPIR), though project FreeFORM (15SIB01).

Appendix A. Supplementary data

Supplementary data related to this article can be found at https://doi.org/10.1016/j.actamat.2018.07.059.

References

[1] T. Ikehara, T. Tsuchiya, Crystal orientation-dependent fatigue characteristics in micrometer-sized single-crystal silicon, Microsyst. Nanoeng. 2 (2016) 16027.
[2] K. Sato, T. Yoshioka, T. Ando, M. Shikida, T. Kawabata, Tensile testing of silicon film having different crystallographic orientations carried out on a silicon chip, Sensor Actuator Phys. 70 (1) (1998) 148–152.
[3] Z.F. Yue, Z.Z. Lu, C.Q. Zheng, Evaluation of creep damage behavior of nickel-base directionally solidified superalloys with different crystallographic orientations, Theor. Appl. Fract. Mech. 25 (2) (1996) 127–138.
[4] T.M. Pollock, Alloy design for aircraft engines, Nat. Mater. 15 (2016) 809.
[5] B.L. Adams, S.I. Wright, K. Kunze, Orientation imaging: the emergence of a new microscopy, Metall.Trans. A 24 (4) (1993) 819–831.
[6] R. Borrajo-Pelaez, P. Hedström, Recent developments of crystallographic analysis methods in the scanning electron microscope for applications in metallurgy, Crit. Rev. Solid State Mater. Sci. (2017) 1–20.
[7] F.J. Humphreys, Review Grain and subgrain characterisation by electron backscatter diffraction, J. Mater. Sci. 36 (16) (2001) 3833–3854.
[8] S. Zaefferer, New developments of computer-aided crystallographic analysis in transmission electron microscopy, J. Appl. Crystallogr. 33 (1) (2000) 10–25.
[9] D. Viladot, M. VÉRon, M. Gemmi, F. PeirÓ, J. Portillo, S. EstradÉ, J. Mendoza, N. Llorca-Isern, S. Nicolopoulos, Orientation and phase mapping in the transmission electron microscope using precession-assisted diffraction spot recognition: state-of-the-art results, J. Microsc. 252 (1) (2013) 23–34.
[10] P.L. Ryder, W. Pitsch, The uniqueness of orientation determination by selected area electron diffraction, Philos. Mag. A: J. Theor. Exp. Appl. Phys. 15 (135) (1967) 437–446.
[11] I. Shozo, Some new techniques in reflection high energy electron diffraction (RHEED) application to surface structure studies, Jpn. J. Appl. Phys. 16 (6) (1977) 891.
[12] R.R. Keller, R.H. Geiss, Transmission EBSD from 10 nm domains in a scanning electron microscope, J. Microsc. 245 (3) (2012) 245–251.
[13] X. Tao, A. Eades, Errors, artifacts, and improvements in EBSD processing and mapping, Microsc. Microanal. 11 (1) (2005) 79–87.
[14] B.E. Warren, X-ray diffraction methods, J. Appl. Phys. 12 (5) (1941) 375–384.
[15] J.S. Richard, L. Wenqi, C. Jethro, C. Matt, G.S. Michael, D.S. Steve, Spatially resolved acoustic spectroscopy for rapid imaging of material microstructure and grain orientation, Meas. Sci. Technol. 25 (5) (2014) 055902.
[16] P. Dunsmuir, The use of polarized light for the examination of etched metal crystals and their orientation, Br. J. Appl. Phys. 3 (8) (1952) 264.
[17] M. Seita, M. Volpi, S. Patala, I. McCue, C.A. Schuh, M.V. Diamanti, J. Erlebacher, M.J. Demkowicz, A high-throughput technique for determining grain boundary character non-destructively in microstructures with through-thickness grains, Npj Computational Materials 2 (2016) 16016.
[18] M. Seita, M.M. Nimerfroh, M.J. Demkowicz, Acquisition of partial grain orientation information using optical microscopy, Acta Mater. 123 (2017) 70–81.
[19] D. Lausch, M. Gläser, C. Hagendorf, Determination of crystal grain orientations by optical microscopy at textured surfaces, J. Appl. Phys. 114 (19) (2013) 194509.
[20] J. Mitchell-Smith, A. Speidel, J. Gaskell, A.T. Clare, Energy distribution modulation by mechanical design for electrochemical jet processing techniques, Int. J. Mach. Tool Manufact. 122 (November 2017) 32–46.
[21] J.A. McGeough, Electrochemical Machining, Kirk-othmer Encyclopedia of Chemical Technology, John Wiley & Sons, Inc, 2000.
[22] C.J. Park, M.M. Lohrengel, T. Hamelmann, M. Pilaski, H.S. Kwon, Grain-dependent passivation of surfaces of polycrystalline zinc, Electrochim. Acta 47 (21) (2002) 3395–3399.
[23] J.H. Seo, J.-H. Ryu, D.N. Lee, Formation of crystallographic etch pits during AC etching of aluminum, J. Electrochem. Soc. 150 (9) (2003) B433–B438.
[24] M. Zamin, M.B. Ives, Effect of chloride lon concentration on the anodic dissolution behavior of nickel, Corrosion 29 (8) (1973) 319–324.
[25] M. Pourbaix, Significance of protection potential in pitting and intergranular corrosion, Corrosion 26 (10) (1970) 431–438.
[26] J. Srinivasan, R.G. Kelly, One-dimensional pit experiments and modeling to determine critical factors for pit stability and repassivation, J. Electrochem. Soc. 163 (13) (2016) C759–C767.
[27] J.R. Galvele, Transport processes and the mechanism of pitting of metals, J. Electrochem. Soc. 123 (4) (1976) 464–474.
[28] R.C. Newman, E.M. Franz, Growth and repassivation of single corrosion pits in stainless steel, Corrosion 40 (7) (1984) 325–330.
[29] B. Zaid, D. Saidi, A. Benzaid, S. Hadji, Effects of pH and chloride concentration on pitting corrosion of AA6061 aluminum alloy, Corrosion Sci. 50 (7) (2008) 1841–1847.
[30] K.P. Rajurkar, D. Zhu, J.A. McGeough, J. Kozak, A. De Silva, New developments in electro-chemical machining, CIRP Ann. - Manuf. Technol. 48 (2) (1999) 567–579.
[31] J.P. Hoare, Oxide film studies on iron in electrochemical machining electrolytes, J. Electrochem. Soc. 117 (1) (1970) 142–145.
[32] J.F. Wilson, Practice and Theory of Electrochemical Machining, Wiley-Interscience, New York, 1971.
[33] M. Datta, D. Landolt, Surface brightening during high rate nickel dissolution in nitrate electrolytes, J. Electrochem. Soc. 122 (11) (1975) 1466–1472.
[34] D.V.V. Moll, R.C. Salvarezza, H.A. Videla, A.J. Arvia, The pitting corrosion of nickel in different electrolyte solutions containing chloride ions, J. Electrochem. Soc. 132 (4) (1985) 754–760.
[35] R. Smith, S. Sharples, W. Li, M. Clark, M. Somekh, Orientation imaging using spatially resolved acoustic spectroscopy, J. Phys. Conf. 353 (1) (2012) 012003.
[36] R. Su, Y. Wang, J. Coupland, R.K. Leach, On tilt and curvature dependent errors and the calibration of coherence scanning interferometry, Optic Express 25 (4) (2017) 3297–3310.

[37] P. Ekberg, R. Su, R.K. Leach, High-precision lateral distortion measurement and correction in coherence scanning interferometry using an arbitrary surface, Optic Express 25 (16) (2017) 18703–18712.
[38] P. de Groot, Principles of interference microscopy for the measurement of surface topography, Adv. Optic Photon 7 (1) (2015) 1–65.
[39] N.R. Pal, S.K. Pal, A review on image segmentation techniques, Pattern Recogn. 26 (9) (1993) 1277–1294.
[40] M. Yasuda, F. Weinberg, D. Tromans, Pitting corrosion of Al and Al-Cu single crystals, J. Electrochem. Soc. 137 (12) (1990) 3708–3715.
[41] H. Kaesche, Microtunnelling during selective alloy dissolution and during pitting, Mater. Corros. 39 (4) (1988) 153–161.
[42] J.F.B.J.A. Lillard, D.G. Kolman, Morphology of pits in nickel: anisotropic growth due to crystallographic orientation, in: M. Seo, H. Takahashi (Eds.), Proceedings/[Electrochemical Society], Electrochemical Society, 1999, pp. 453–462.
[43] M. Baumgärtner, H. Kaesche, Aluminum pitting in chloride solutions: morphology and pit growth kinetics, Corrosion Sci. 31 (1990) 231–236.
[44] T.B. Britton, J. Jiang, Y. Guo, A. Vilalta-Clemente, D. Wallis, L.N. Hansen, A. Winkelmann, A.J. Wilkinson, Tutorial: crystal orientations and EBSD — or which way is up? Mater. Char. 117 (2016) 113–126.
[45] D. Landolt, Fundamental aspects of electropolishing, Electrochim. Acta 32 (1) (1987) 1–11.
[46] T. Kawanaka, M. Kunieda, Mirror-like finishing by electrolyte jet machining, CIRP Ann. - Manuf. Technol. 64 (1) (2015) 237–240.
[47] N.A. Lange, Lange's Handbook of Chemistry, fifteenth ed., McGraw-Hill, New York, 1999.
[48] M. Schneider, S. Schroth, S. Richter, S. Höhn, N. Schubert, A. Michaelis, In-situ investigation of the interplay between microstructure and anodic copper dissolution under near-ECM conditions—Part 2: the transpassive state, Electrochim. Acta 70 (2012) 76–83.
[49] D. Landolt, Throwing power measurements during high rate nickel dissolution under active and transpassive conditions, J. Electrochem. Soc. 119 (6) (1972) 708–712.
[50] R.K. Leach, Optical Measurement of Surface Topography, Springer-Verlag, Berlin, 2011.